CHARACTERIZATION OF ANISOTROPIC IRREGULAR ROUGHNESS THROUGH DIRECT NUMERICAL SIMULATIONS

Jiasheng Yang
Institute of Fluid Mechanics
Karlsruhe Institute of Technology
Karlsruhe, Germany
jiasheng.yang@kit.edu

Alexander Stroh
Institute of Fluid Mechanics
Karlsruhe Institute of Technology
Karlsruhe, Germany
alexander.stroh@kit.edu

Shervin Bagheri
FLOW Centre
Royal Institute of Technology (KTH)
Stockholm, Sweden
shervin@mech.kth.se

Bettina Frohnapfel
Institute of Fluid Mechanics
Karlsruhe Institute of Technology
Karlsruhe, Germany
bettina.frohnapfel@kit.edu

Pourya Forooghi
Department of Mechanical & Production Engineering
Aarhus University
Aarhus, Denmark
forooghi@mpe.au.dk

ABSTRACT

Surfaces on flow-related equipment are often hydraulically rough due to diverse degradation processes. The formation of roughness may demonstrate directional preference, influenced by factors such as operational conditions. While research on irregular roughness in the past few decades has predominantly adhered to the assumption of surface isotropy, our current study takes a novel approach by delving into systematic research on the effect of roughness anisotropy across various scales. To achieve this, we generate irregular anisotropic roughness based on 2-D power spectra (PS) with directional preferences. It is noteworthy that the anisotropic surfaces under investigation share either identical surface anisotropy ratio (SAR=L_x^{Corr}/L_z^{Corr}) or effective slope ratio (ESR=ES_x/ES_z) and roughness height probability density function (PDF). Through diverse manipulations of the 2-D PS, the degree of roughness anisotropy at different scales is individually manipulated. Direct numerical simulations of turbulent channel flows over these anisotropic rough surfaces are conducted at $Re_\tau = 500$. The present investigation underscores the pivotal roles played by the multi-scale nature and directional attributes of irregular anisotropic surfaces to the resulting drag. Additionally, this study demonstrates the insufficiency of the known roughness statistics in accurately reflecting these factors. In light of this, we introduce a novel statistical metric that shows promise in effectively scaling the anisotropic effect. The efficacy of this metric is examined through an analysis of both the existing database and literature on anisotropic roughness.

1 Introduction

Hydraulically rough surfaces can be frequently observed in flow-related realistic applications. Predicting roughness-induced skin friction is of crucial economic and ecological significance, especially for the industries relying on transportation. The development of a universally applicable predictive correlation for the impact of roughness remains a formidable challenge due to the inherent multi-scale and stochastic nature of roughness characteristics. Over the past few decades, significant endeavors have been devoted to the characterization

of roughness drag solely based on their topographical properties. The pioneering work traces back to Nikuradse (1933), who demonstrated a correlation between the height of uniform sand grains and their skin friction coefficient (C_f). The skin friction coefficient is defined as

$$C_f = \frac{2\tau_w}{\rho U_b^2},$$ (1)

where τ_w represents wall shear stress. According to the outer layer similarity hypothesis by Townsend (1976), which states that outer layer turbulence is unaffected by the near wall roughness perturbations. As a consequence the impact of the roughness on the outer layer flow manifests merely in the downward shift of the mean velocity profile. This offset in the logarithmic layer is anticipated to be constant in the outer layer and is denoted as the (Hama) roughness function ΔU^+ (Hama, 1954). Thus the logarithmic law in the context of surface roughness reads

$$U^+ = \frac{1}{\kappa} \ln y^+ + B - \Delta U^+.$$ (2)

Here $\kappa \approx 0.41$ denotes the von Kármán constant and $B = 5.2$ is the intersect of the log-law. Based on the outer layer similarity hypothesis and the assumption of negligible deviation of viscous and buffer layer velocity profile from the idealized velocity profile, the skin friction coefficient of the rough surface ($C_{f,r}$) can be used to estimate ΔU^+ via (Frohnapfel et al., 2024)

$$\Delta U^+ = \frac{1}{\kappa} \ln \sqrt{\frac{C_{f,r}}{C_{f,s}}} + \sqrt{\frac{2}{C_{f,s}}} - \sqrt{\frac{2}{C_{f,r}}}.$$ (3)

Here, $C_{f,s}$ represents skin friction of smooth surface at identical Re_b.

In the context of irregular roughness, various single-valued roughness statistical parameters are proposed in the literature to reflect the degree of roughness. Based on these statistical parameters, machine learning models are built, see e.g. (Jouybari *et al.*, 2021; Lee *et al.*, 2022). One of the influential parameters is the effective slope ES, which is defined as (Napoli *et al.*, 2008)

$$\text{ES}_x = \left\langle \frac{\partial k}{\partial x} \right\rangle \quad \text{and} \quad \text{ES}_z = \left\langle \frac{\partial k}{\partial z} \right\rangle, \qquad (4)$$

where k represents roughness height map as a function of wall-parallel coordinates x and z, $\langle \cdot \rangle$ indicates spatial averaging within the plane. As another example, the correlation lengths $L_{x,z}^{Corr}$ are defined as the lengths of roughness at which the auto-correlation of roughness decreases to 0.2 in the x and z directions, respectively. (Thakkar *et al.*, 2017). Alternatively, Yang *et al.* (2022) utilized a different characterization approach involving roughness height probability density function (PDF) and 1-D power spectrum (PS). This methodology enables the successful replication of skin friction of realistic roughness through artificial roughness with matched PDF and PS (Yang *et al.*, 2023b). In their latest work, a data-driven predictive model based on PDF and PS characterization is developed, achieving outstanding level of predictive performance over a broad types of irregular roughness (Yang *et al.*, 2023a). Nevertheless, it is imperative to recognize that a considerable body of previous research has primarily operated under the presumption of rough surface isotropy. Here the surface isotropy presumption indicates that the surface statistics – e.g. ES – manifest no difference in any wall-parallel directions. Consequently, it is anticipated that the roughness effect – albeit the stochastic nature of the most irregular rough surfaces – is invariant in terms of its in-plane orientation. Departing from this premise, the notable influence of surface anisotropy has been reported in the literature, e.g. in Busse & Jelly (2020); Jelly *et al.* (2022). In their investigations, the anisotropy of the artificial roughness is realized by independently varying the cut-off lengths of the exponential roughness height correlation functions in the spanwise and streamwise directions, thereby leading to a similar degree of anisotropy across varying length scales. The notable variation in the impact of roughness on the flow is evidently dependent on the directional preference of the roughness structures. Motivated by these works, the present study embark on a systematic investigation of roughness structures that manifest varying degrees of anisotropy across distinct length scales. To this end, we employ the 2-D anisotropic PS representation method to construct a roughness database encompassing systematically varied roughness anisotropy. Subsequently, in-depth investigation of turbulent flow behaviors at $\text{Re}_\tau = 500$ over these roughness geometries is conducted through direct numerical simulations (DNS).

2 Methodology
2.1 Anisotropic roughness generation

In the present work, artificial irregular rough surfaces are generated through a mathematical random roughness generation method where the PS and PDF of the roughness can be prescribed (Pérez-Ràfols & Almqvist, 2019). The applicability of this generation method for generating isotropic realistic surface surrogates based on 1-D PS profile is demonstrated in our previous publication (Yang *et al.*, 2023b). The roughness structures are represented by 2-D discrete elevation maps
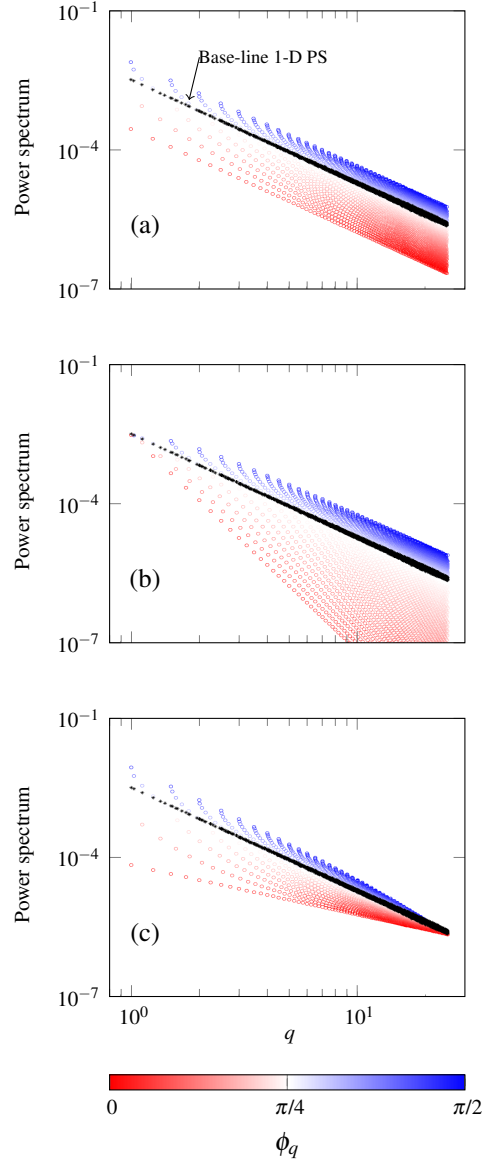

Figure 1: Illustrations of 2-D PS as functions of $q = \sqrt{q_p^2 + q_s^2}$ for (a) $\mathscr{C}_{\text{Shift}}$, (b) $\mathscr{C}_{\text{q0}}$ and (c) $\mathscr{C}_{\text{q1}}$. Color indicates ϕ_q, Black symbols represent the base-line 1-D PS profile.

as functions of wall-parallel coordinates $k(x,z)$. In the current database, $k_{99} = 0.1H$ is consistently achieved, where H indicates the channel half height. Consistent with the previous publication utilizing the same generation algorithm (Yang *et al.*, 2022), extreme roughness peaks or valleys are truncated beyond $1.2 \times k_{99}$ around k_{md}, where k_{99} represents the 99% confidence interval of the PDF and $k_{md} = \int_S k \, dS / S$ denotes the roughness melt-down height measured from the lowest roughness valley. $k_{99} = 0.1H$ is achieved throughout the current database, where H indicates channel half height.

Initially, the reference isotropic roughness $\mathscr{C}_{\text{Ref}}$ is introduced based on the base-line 1-D power-law PS: $E_k(q) = C_0(\|q\|/q_0)^p$ where q is the wavenumber, $q_0 = 2\pi/\lambda_0$ is the smallest wavenumber corresponding to the largest in-plane roughness length scale $\lambda_0 = 2H$, C_0 is a constant to scale the roughness height, and $p = 2.5$ is the spectral slope of PS. Following this definition, anisotropic 2-D PS are constructed. First of all, the primary and secondary directions are defined

Case		SAR	ESR	k_t/H	ES_x	ES_z	L_x^{Corr}/H	L_z^{Corr}/H	ΔU^+	$\Delta U_{Eqn.3}^+$	$C_f \times 100$
Isotropic	$\mathscr{C}_{Ref}$	1.0	1.0	0.12	0.24	0.24	0.31	0.30	5.53	5.53	1.30
Streamwise	$\mathscr{C}_{Shift,x}^{SAR}$	3.10	0.55	0.12	0.16	0.29	0.65	0.21	4.22	4.23	1.07
	$\mathscr{C}_{q0,x}^{SAR}$	3.00	0.44	0.12	0.14	0.32	0.45	0.15	4.09	4.11	1.05
	$\mathscr{C}_{q1,x}^{SAR}$	3.23	0.77	0.12	0.20	0.26	0.71	0.22	4.47	4.48	1.11
	$\mathscr{C}_{Shift,x}^{ESR}$	1.56	0.77	0.12	0.20	0.26	0.39	0.25	5.00	4.99	1.20
	$\mathscr{C}_{q0,x}^{ESR}$	1.10	0.77	0.12	0.20	0.27	0.32	0.29	5.15	5.18	1.23
Spanwise	$\mathscr{C}_{Shift,z}^{SAR}$	0.33	1.88	0.12	0.30	0.16	0.20	0.61	6.42	6.46	1.52
	$\mathscr{C}_{q0,z}^{SAR}$	0.34	2.29	0.12	0.32	0.14	0.15	0.44	6.40	6.42	1.51
	$\mathscr{C}_{q1,z}^{SAR}$	0.31	1.30	0.12	0.26	0.20	0.20	0.64	6.07	6.10	1.43
	$\mathscr{C}_{Shift,z}^{ESR}$	0.66	1.27	0.12	0.26	0.21	0.25	0.38	5.95	5.96	1.40
	$\mathscr{C}_{q0,z}^{ESR}$	0.88	1.30	0.12	0.26	0.20	0.28	0.32	5.85	5.86	1.38

Table 1: Statistics of investigated roughness along with their skin friction coefficient C_f. ESR=ES_x/ES_z denotes the ratio of streamwise and spanwise effective slopes. The colored blocks indicate the values that are kept consistent across different cases.

on the 2-D PS map with coordinate q_p and q_s, respectively. It is worth mentioning that the primary and secondary directions are oriented perpendicularly in the 2-D PS-plane. The angular coordinate is calculated by $\phi_q = \tan^{-1}(q_s/q_p)$. The base-line 1-D PS profile is assigned for the 2-D PS map along $\phi_q = \pi/4$. Subsequently, to achieve different anisotropic behavior, three types of PS profile adjustments in the primary direction – i.e. along $\phi_q = 0$ – are employed and denoted with the corresponding abbreviations:

1. $\mathscr{C}_{Shift}$: shifting the base-line PS profile
2. $\mathscr{C}_{q0}$: adjusting PS slope p while maintaining identical PS at lowest in-plane roughness wavenumber q_0
3. $\mathscr{C}_{q1}$: adjusting PS slope p while maintaining identical PS at highest in-plane roughness wavenumber q_1

Here the primary direction $\phi_q = 0$ can be placed either in streamwise direction (denoted with subscript x) or spanwise direction (denoted with subscript z) to generate differently oriented anisotropic roughness. On the other hand, the PS in the secondary direction, $\phi_q = \pi/2$, is determined accordingly to ensure that the resulting azimuthally averaged 2-D PS matches the base-line 1-D PS profile. Following which, the first quarter of the 2-D PS – i.e. within $\phi_q = [0, \pi/2]$ – is constructed through azimuthal interpolation based on the three pre-defined 1-D profiles on $\phi_q = 0$, $\phi_q = \pi/4$ and $\phi_q = \pi/2$. The rest part of the 2-D PS map, i.e. $\phi_q \in]\pi/2, 2\pi[$ is obtained by mirroring the known quarter of the PS. An illustration of the three aforementioned types of 2-D anisotropic PS is depicted in figure 1. The exemplary roughness corresponding to each considered roughness case are depicted in figure 2.

The surface anisotropy ratio (SAR=L_x^{Corr}/L_z^{Corr}) (Busse & Jelly, 2020) serves as a measure of the degree of overall surface anisotropy. SAR$\approx$ 3 (or the reversed values for the spanwise cases) are kept consistent across the investigated cases with superscript SAR. Additionally, the impact of the ratio of effective slopes in the streamwise and spanwise directions ESR=ES_x/ES_z are investigated by adjusting $\mathscr{C}_{Shift}$ and $\mathscr{C}_{q0}$ surfaces to achieve the same ESR values as that of $\mathscr{C}_{q1}^{SAR}$. These cases are labeled with the superscript ESR. The resulting roughness statistics are illustrated in table 1
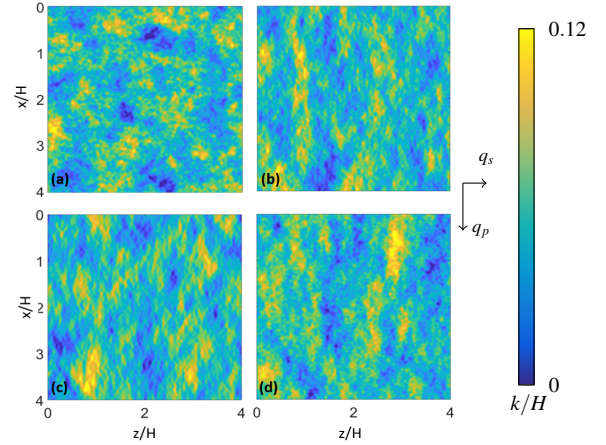

Figure 2: Exemplary roughness height distribution for different types of surface anisotropy, (a) $\mathscr{C}_{Ref}$ (isotropic reference), (b) $\mathscr{C}_{Shift}$, (c) $\mathscr{C}_{q1}$ and (d) $\mathscr{C}_{q0}$. Please note that the flow direction is either along q_s or q_r among the considered cases.

2.2 Direct numerical simulation

Direct Numerical Simulations (DNS) are carried out in fully developed turbulent channels driven by constant pressure gradient (CPG) with the spectral solver SIMSON (Chevalier *et al.*, 2007). Within the channel, identical roughness patches are installed on both upper and lower wall as illustrated in figure 3. The Navier-Stokes equation writes:

$$\nabla \cdot \mathbf{u} = 0, \tag{5}$$

$$\frac{\partial \mathbf{u}}{\partial t} + \nabla \cdot (\mathbf{uu}) = -\frac{1}{\rho}\nabla p + \nu\nabla^2 \mathbf{u} - \frac{1}{\rho}P_x e_x + \mathbf{f}_{IBM}, \tag{6}$$

where ρ, ν represent the density, the kinematic viscosity of the flow, respectively. The roughness with no-slip boundary and zero-temperature boundary conditions are realized by imposing immersed boundary method (IBM) following Gold-
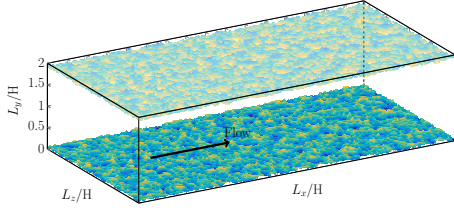
Figure 3: Schematic representation of simulation domain with an exemplary rough surface mounted on the channel walls.

Figure 5: Mean velocity deficit profile, line styles correspond to figure 4
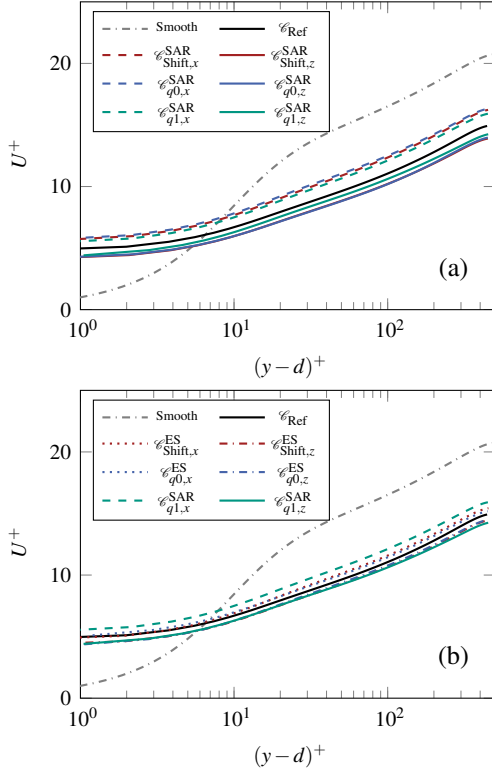

(a)

(b)

Figure 4: DNS results of considered cases. The color indicates different types of roughness anisotropy. The inner-scaled mean velocity profiles are compared among the cases with same (a) SAR and (b) ESR.

stein *et al.* Goldstein *et al.* (1993). Thus, external source terms for momentum ($\mathbf{f}_{\text{IBM}}$) is added in the equation. P_x indicates the constant pressure gradient in the flow direction. The value of P_x is predefined to achieve $\text{Re}_\tau = u_\tau \text{H}_{\text{eff}}/\nu = 500$. Here $u_\tau = \sqrt{\tau_w/\rho}$ denotes friction velocity, $\tau_w = P_x \text{H}_{\text{eff}}$ is the wall shear stress corresponding to the effective channel height $\text{H}_{\text{eff}} = \text{H} - k_{md}$. The dimension of the DNS domain is $(L_x, L_y, L_z) = (8\text{H}, 2\text{H}, 4\text{H})$.

3 Results
3.1 Impact of anisotropic roughness

The DNS results, specifically the inner-scaled mean velocity profiles U^+ are obtained by applying averaging in wall-parallel directions and time. The mean velocity profiles are illustrated in figure 4 as functions of $(y-d)^+$, here the virtual
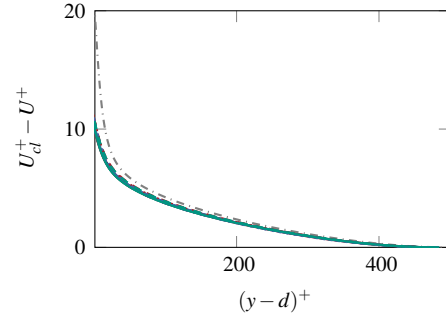
origin of the rough wall is determined by the zero-plane displacement d following Jackson (1981). Moreover, we include $\mathscr{C}_{\text{Ref}}$ in the figure with the solid black line. The substantial deviations observed in U^+ relative to $\mathscr{C}_{\text{Ref}}$ underscore the significance of accounting for surface anisotropy when characterizing arbitrary irregular roughness. Additionally, the deficit mean velocity profiles are depicted in figure 5. It can be observed that that outer layer similarity is evident only above the level $(y-d)^+ \gtrsim 100$, which is slightly higher than typical values reported in the literature. This phenomenon, nevertheless, aligns with the observations from preceding studies, suggesting that the wall-normal extent of the roughness sublayer may extend to higher levels due to multiple factors associated with the roughness topography, such as with the large spanwise wavelength (Chan *et al.*, 2018).

The C_f as well as the ΔU^+ values are computed for each case and are documented on the right most columns of table 1. Moreover, the values of ΔU^+ calculated through Eqn. 3, denoted as $\Delta U^+_{Eqn.3}$, are shown as well. It is evident that the roughness function calculated through Eqn. 3 serves as an accurate estimation of which obtained through comparing the velocity profile offset. This indicates that the variation of the global skin friction coefficient C_f can be rather accurately captured by ΔU^+ with a maximum deviation lower than 1%, despite the non-negligible deviation observed in the current velocity profiles from the ideal form, e.g. the violation of outer layer similarity to some degree. The ΔU^+ values calculated directly from the velocity offset will be used in the following content.

The ΔU^+ values are plotted in figure 6(a) against SAR. In the figure, different types of the roughness anisotropy are distinguished by symbol color, the base-line isotropic case is included with black circle. Similarly to the previous observations, the variation of ΔU^+ is evident between streamwise and spanwise aligned roughness. Generally, the ΔU^+ values decrease with SAR. The impact of surface anisotropy of different types are obvious, yet to distinguishable extend. The variation of ΔU^+ of the streamwise anisotropic roughness (SAR> 1) can be clearly observed. The $\mathscr{C}_{q0,x}^{\text{SAR}}$ and $\mathscr{C}_{q0,x}^{\text{ESR}}$ cases demonstrate the most significant decrease in ΔU^+ with increasing SAR, while $\mathscr{C}_{q1,x}^{\text{SAR}}$ achieves the least decrease in ΔU^+ under similar SAR condition. In the cases of spanwise anisotropy (SAR < 1), a similar conclusion can be drawn, whereby ΔU^+ exhibits lowest sensitivity to SAR for $\mathscr{C}_{q1,z}^{\text{SAR}}$. However, the increase of ΔU^+ for $\mathscr{C}_{q0,z}^{\text{SAR}}$ seems saturated when compared with $\mathscr{C}_{\text{shift},z}^{\text{SAR}}$, this could be attributed to the approach to the rough regime as evident in its ES_x value (Schultz & Flack, 2009). The observed difference in the variation of ΔU^+ across different types of anisotropy can be attributed to the distinct
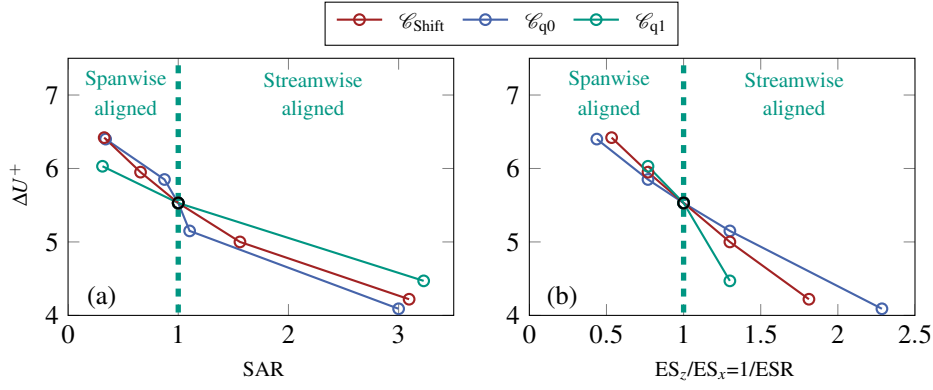
Figure 6: The roughness function, ΔU^+, plotted as functions of the (a)SAR, (b) ES_z/ES_x=1/ESR. The color indicates different types of roughness anisotropy. The reference case $\mathscr{C}_{Ref}$ is represented by black circle.
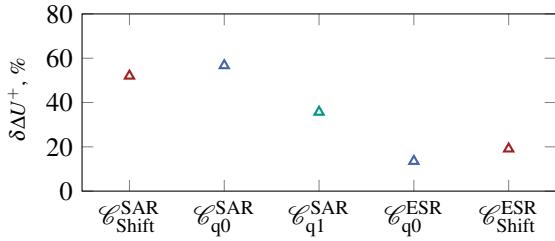

Figure 7: $\delta\Delta U^+$ of different types of surface anisotropy.

Figure 8: The roughness function, ΔU^+, plotted against ESR/SAR.

types of roughness anisotropy. Among the examined cases illustrated in figure 1, $\mathscr{C}_{q1}$ gradually converges towards the base-line isotropic state at smaller wavelengths. In contrast, $\mathscr{C}_{q0}$ displays a divergent behavior of PS at large wavenumbers, resulting in elongated small-scale structures. This disparity underscores the significant influence of small-scale roughness structures on skin friction.

Having recognised the limitations of SAR in accurately representing the surface anisotropy, the correlation between ΔU^+ and ES_z/ES_x is depicted in figure 4(b). it should be noted that the abscissa of this figure ES_z/ES_x=1/ESR, which is adopted from the investigation by Jelly *et al.* (2022). Additionally, these anisotropic cases are connected with the reference case $\mathscr{C}_{ref}$, due to the fact that the entire database is generated based on the base-line 1-D PS. It can be seen from this figure that ΔU^+ undergoes more linear transitions, albeit with distinct slopes for each anisotropy type. Nevertheless, despite the observed trends, the variance in ΔU^+ within the current characterization of surface anisotropy remains significant. This observation implies that these single-valued parameters may not fully encapsulate the multi-scale complexity of roughness, particularly in representing the varying effects of roughness anisotropy across different length scales.

Moreover, the percentage variation of ΔU^+ between spanwise-aligned roughness (ΔU_z^+) and streamwise-aligned roughness(ΔU_x^+) is expressed as $\delta\Delta U^+ = 100 \times \frac{\Delta U_z^+ - \Delta U_x^+}{\Delta U_x^+}$ and depicted in figure 7 grouped by the type of surface anisotropy. It is evident that $\mathscr{C}_{Shift}^{SAR}$ and $\mathscr{C}_{q0}^{SAR}$ exhibit similar values of $\delta\Delta U^+ = 52\%$ and 57%, respectively, while $\delta\Delta U^+$ for $\mathscr{C}_{q1}^{SAR}$ is notably lower with $\delta\Delta U^+ = 19\%$ and 14%, respectively. This suggests that the drag is more sensitive to the anisotropy of the relatively small-scale roughness structures (corresponding to the structures at high wavenumbers). On the other hand, the cases with consistent ESR values, namely $\mathscr{C}_{Shift}^{ESR}$ and $\mathscr{C}_{q0}^{ESR}$,
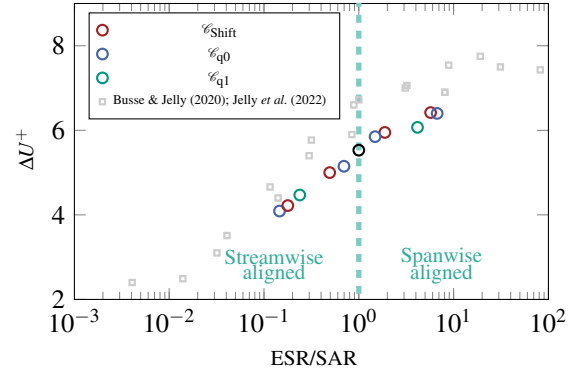
exhibit lower skin-friction difference which can be attributed to the significant lower degree of anisotropy as reflected by their SAR values.

3.2 Characterization of surface anisotropy

Before proceeding with the characterization of the hydrodynamic properties of roughness in regard to the current measurements of surface anisotropy – namely SAR and ESR – it is crucial to discuss the topographical implications of these parameters. As shown in table 1, similar SAR values are obtained for different types of anisotropy, while $\mathscr{C}_{q1}^{SAR}$ exhibits the ESR value closest to unity. However, conversely, for the cases with similar ESR values, $\mathscr{C}_{q0}^{ESR}$ shows the SAR value closest to unity. This indicates that ES and L^{Corr} – and consequently ESR and SAR – are primarily influenced by relatively small- and large-scale structures, respectively. Bearing this in mind, the significant scattering of ΔU^+ when plotted against SAR or ESR in figure 6 underscores the combination of the impact of anisotropy at various length scales on the resulting roughness skin friction. A new characterization parameter for roughness anisotropy is thus defined as

$$\frac{ESR}{SAR} = \frac{\langle\frac{\partial k}{\partial x}\rangle \times L_z^{Corr}}{\langle\frac{\partial k}{\partial z}\rangle \times L_x^{Corr}} . \qquad (7)$$

The values of ΔU^+ for all investigated cases are plotted against ESR/SAR in Figure 8. It is evident that the analyzed data exhibit a clear collapse onto a single line, despite their varied

forms of anisotropy. The anisotropic roughness data from previous studies (Jelly *et al.*, 2022; Busse & Jelly, 2020) are depicted in the same plot. All integrated data exhibit a consistent trend as a function of ESR/SAR. The systematic offset of ΔU^+ compared with the current database and the scattering of ΔU^+ within the literature database are likely attributed to variations in the hydrodynamic characteristics of their respective base-line isotropic roughness, e.g. in the roughness height and PS. This is to say that the literature data may not all originate from the same base-line isotropic roughness in a manner similar to that outlined in the present work. The influence of this variation in the hydrodynamic properties of the base-line isotropic roughness can be discerned from the scattering of ΔU^+ in figure 8 at ESR/SAR ≈ 1.

4 Conclusion

In this study, DNSs are performed to analyze turbulent flow over irregular anisotropic roughness at $\mathrm{Re}_\tau = 500$, focusing on three types of surface anisotropy – denoted as $\mathscr{C}_{\mathrm{Shift}}$, $\mathscr{C}_{\mathrm{q0}}$, and $\mathscr{C}_{\mathrm{q1}}$. These three types of surface anisotropy exhibit different anisotropic properties and are obtained by means of systematically manipulated 2-D PS. Despite different types of surface anisotropy, the values of SAR or ESR are kept constant across the roughness by adjusting the degree of anisotropy in the 2-D PS. Here SAR is defined as the ratio of streamwise (L_x^{Corr}) to spanwise (L_z^{Corr}) correlation lengths, while ESR is calculated as the ratio of streamwise (ES_x) to spanwise (ES_z) effective slopes. The impact of these anisotropic roughness structures, which are aligned either parallel and perpendicular to the flow direction, are investigated. The impact of surface anisotropy across diverse length scales on resulting skin friction is observed in the present work. This impact is reflected in the variation of the percentage change in the roughness function, denoted as $\delta \Delta U^+$, between streamwise- and spanwise-aligned roughness of different anisotropic types. These variation ranges from 36% to 57% for the roughness with corresponding SAR values and from 14% to 36% for the ESR counterpart respectively. Moreover, we utilized SAR and $\mathrm{ES}_z/\mathrm{ES}_z$ for capturing the impact of surface anisotropy on the resulting skin friction. It is evident that these parameters alone are insufficient to fully represent the effect of various types of anisotropic roughness on the variation of the skin friction. A new parameter ESR/SAR is proposed in the present work to characterize the degree of surface anisotropy. This parameter is demonstrated to effectively capture the impact of distinct types of variation in the 2-D PS on the alteration of roughness skin friction. Further examination of this parameter on a broader types of rough surfaces is called in future research to enhance the understanding of its implications on the mechanism of roughness-induced skin friction.

Acknowledgements

REFERENCES

Busse, A. & Jelly, T. O. 2020 Influence of surface anisotropy on turbulent flow over irregular roughness. *Flow Turbul. Combust.* **104**, 331 – 354.

Chan, L., MacDonald, M., Chung, D., Hutchins, N. & Ooi, A. 2018 Secondary motion in turbulent pipe flow with three-dimensional roughness. *Journal of Fluid Mechanics* **854**, 5–33.

Chevalier, M, Schlatter, P., Lundbladh, A & Henningson, D. 2007 SIMSON–A pseudo-spectral solver for incompressible boundary layer flow. *Tech. Rep. TRITA-MEK 2007:07, KTH, Stockholm, Sweden* pp. 1–100.

Frohnapfel, Bettina, von Deyn, Lars, Yang, Jiasheng, Neuhauser, Jonathan, Stroh, Alexander, Örlü, Ramis & Gatti, Davide 2024 Flow resistance over heterogeneous roughness made of spanwise-alternating sandpaper strips. *Journal of Fluid Mechanics* **980**, A31.

Goldstein, D., Handler, R. & Sirovich, L. 1993 Modeling a no-slip flow boundary with an external force field. *J. Comput. Phys.* **105** (2), 354–366.

Hama, F.R. 1954 *Boundary-layer Characteristics for Smooth and Rough Surfaces.*

Jackson, P. S. 1981 On the displacement height in the logarithmic velocity profile. *Journal of Fluid Mechanics* **111**, 15–25.

Jelly, T.O., Ramani, A., Nugroho, B., Hutchins, N. & Busse, A. 2022 Impact of spanwise effective slope upon rough-wall turbulent channel flow. *J. Fluid Mech.* **951**, A1.

Jouybari, M. A., Yuan, J., Brereton, G. J. & Murillo, M. S. 2021 Data-driven prediction of the equivalent sand-grain height in rough-wall turbulent flows. *Journal of Fluid Mechanics* **912**, A8.

Lee, S., Yang, J., Forooghi, P., Stroh, A. & Bagheri, S. 2022 Predicting drag on rough surfaces by transfer learning of empirical correlations. *Journal of Fluid Mechanics* **933**, A18.

Napoli, E., Armenio, V. & DeMarchis, M. 2008 The effect of the slope of irregularly distributed roughness elements on turbulent wall-bounded flows. *Journal of Fluid Mechanics* **613**, 385–394.

Nikuradse, J. 1933 *Stroemungsgesetze in rauhen Rohren.* Berlin: VDI-Verl.

Pérez-Ràfols, F. & Almqvist, A. 2019 Generating randomly rough surfaces with given height probability distribution and power spectrum. *Tribol. Int.* **131**, 591 – 604.

Schultz, M. P. & Flack, K. A. 2009 Turbulent boundary layers on a systematically varied rough wall. *Physics of Fluids* **21** (1), 015104.

Thakkar, M., Busse, A. & Sandham, N. 2017 Surface correlations of hydrodynamic drag for transitionally rough engineering surfaces. *Journal of Turbulence* **18** (2), 138–169.

Townsend, A. A. 1976 *The structure of turbulent shear flow / A.A.Townsend*, 2nd edn. Cambridge University Press Cambridge [Eng.] ; New York.

Yang, J., Stroh, A., Chung, D. & Forooghi, P. 2022 Dns-based characterization of pseudo-random roughness in minimal channels. *J. Fluid Mech.* **941**, A47.

Yang, Jiasheng, Stroh, Alexander, Lee, Sangseung, Bagheri, Shervin, Frohnapfel, Bettina & Forooghi, Pourya 2023*a* Prediction of equivalent sand-grain size and identification of drag-relevant scales of roughness – a data-driven approach. *Journal of Fluid Mechanics* **975**, A34.

Yang, J., Velandia., J., Bansmer, S., Stroh, A. & Forooghi, P. 2023*b* A comparison of hydrodynamic and thermal properties of artificially generated against realistic rough surfaces. *Int. J. Heat Fluid Flow* **99**, 109093.